Earth and Planetary Science Letters 563 (2021) 116875

Contents lists available at ScienceDirect

Earth and Planetary Science Letters

www.elsevier.com/locate/epsl

Non-double-couple earthquakes in 2017 swarm in Reykjanes Peninsula, SW Iceland: Sensitive indicator of volcano-tectonic movements at slow-spreading rift

Pavla Hrubcová *, Jana Doubravová, Václav Vavryčuk

Institute of Geophysics, Czech Academy of Sciences, Prague, Czech Republic

ARTICLE INFO

Article history:
Received 16 October 2020
Received in revised form 11 February 2021
Accepted 3 March 2021
Available online 1 April 2021
Editor: H. Thybo

Keywords:
earthquake swarm
moment tensor
non-double-couple components
Reykjanes Peninsula SW Iceland
focal mechanisms
volcano-tectonic evolution

ABSTRACT

The analysis of the 2017 earthquake swarm along the obliquely divergent Reykjanes Peninsula plate boundary revealed the most frequent focal mechanisms corresponding to main activated fault, which relates to transform faulting of the North Atlantic Rift in Iceland. Detailed double-difference locations, focal mechanisms and non-double-couple (non-DC) volumetric components of seismic moment tensors indicate an activation of three fault segments suggesting continuous interactions between tectonic and magmatic processes. They are related to inflation/deflation of a vertical magmatic dike and comprise: (1) shearing at strike-slip transform fault with left lateral motion; (2) collapses at normal faulting with negative volumetric components due to magma/fluid escape, and (3) shear-tensile opening at oblique strike-slip faulting with positive volumetric components connected to flow of trapped over-pressurized fluids. The identification of three regimes of complex volcano-tectonic evolution in divergent plate movement proves an enormous capability of the non-DC volumetric components to map tectonic processes in such settings.

© 2021 The Author(s). Published by Elsevier B.V. This is an open access article under the CC BY-NC-ND license (http://creativecommons.org/licenses/by-nc-nd/4.0/).

1. Introduction

Iceland is situated above the Mid-Atlantic Ridge separating the North American and the Eurasian plates. In the SW, the Reykjanes Peninsula forms a highly oblique spreading segment of the Mid-Atlantic Ridge. In this place, the rift bends to a landward continuation and connects the Mid-Atlantic Ridge to the Icelandic Western Volcanic Zone (Einarsson, 2008). The Reykjanes Peninsula forms a transtensional plate boundary zone characterized by a high seismicity, recent volcanism and high-temperature geothermal fields (Einarsson et al., 2018). The volcanic systems comprise a central volcano linked to magmatic fissures, where a shallow magma transport occurs by means of dikes. These dikes play a fundamental role in controlling the magmatic, structural, and morphological evolution of volcanic edifices by feeding rift zones (Acocella and Neri, 2009).

The mechanisms at divergent rift plate boundaries are complex and include transform faulting, rifting, diking, inflation and deflation of magma chambers, cooling of magma bodies, and volume changes due to geothermal fluids (Einarsson, 2008; Sigmundsson et al., 2014). These processes are traced by seismic activity; thus a proper analysis of earthquakes provides an insight to their understanding. Most seismicity studies assume that earthquakes have double-couple (DC) source mechanisms corresponding to shear motion on planar faults. However, many well-recorded earthquakes have radiation patterns that depart from this model, indicating fundamentally different sources with non-double-couple (non-DC) mechanisms (Frohlich, 1994; Julian et al., 1998). In the volcano-tectonic rift environment such as Iceland, the non-DC components are expected (Nettles and Ekström, 1998; Oliva et al., 2019) and their analysis can contribute to revealing connections between the magma transport and rifting.

The mechanisms of seismic sources can be described by moment tensors (MT), which comprise both DC and non-DC components. The non-DC components can be further decomposed into the isotropic (ISO) and compensated linear vector dipole (CLVD) components (Knopoff and Randall, 1970; Vavryčuk, 2015). The ISO represents a volumetric change in the earthquake source with positive values indicating tensile opening or explosions, and with negative values indicating crack closures or implosions; the CLVD has a complex physical interpretation (Frohlich, 1994; Julian et al., 1998; Vavryčuk, 2015).

The non-DC components are observed in relation to collapses of the volcano caldera (Julian et al., 1998; Dreger et al., 2000; Templeton and Dreger, 2006; Shuler and Ekström, 2009), in volcano-

* Corresponding author.
E-mail addresses: pavla@ig.cas.cz (P. Hrubcová), doubravka@ig.cas.cz (J. Doubravová), vv@ig.cas.cz (V. Vavryčuk).

https://doi.org/10.1016/j.epsl.2021.116875
0012-821X/© 2021 The Author(s). Published by Elsevier B.V. This is an open access article under the CC BY-NC-ND license (http://creativecommons.org/licenses/by-nc-nd/4.0/).

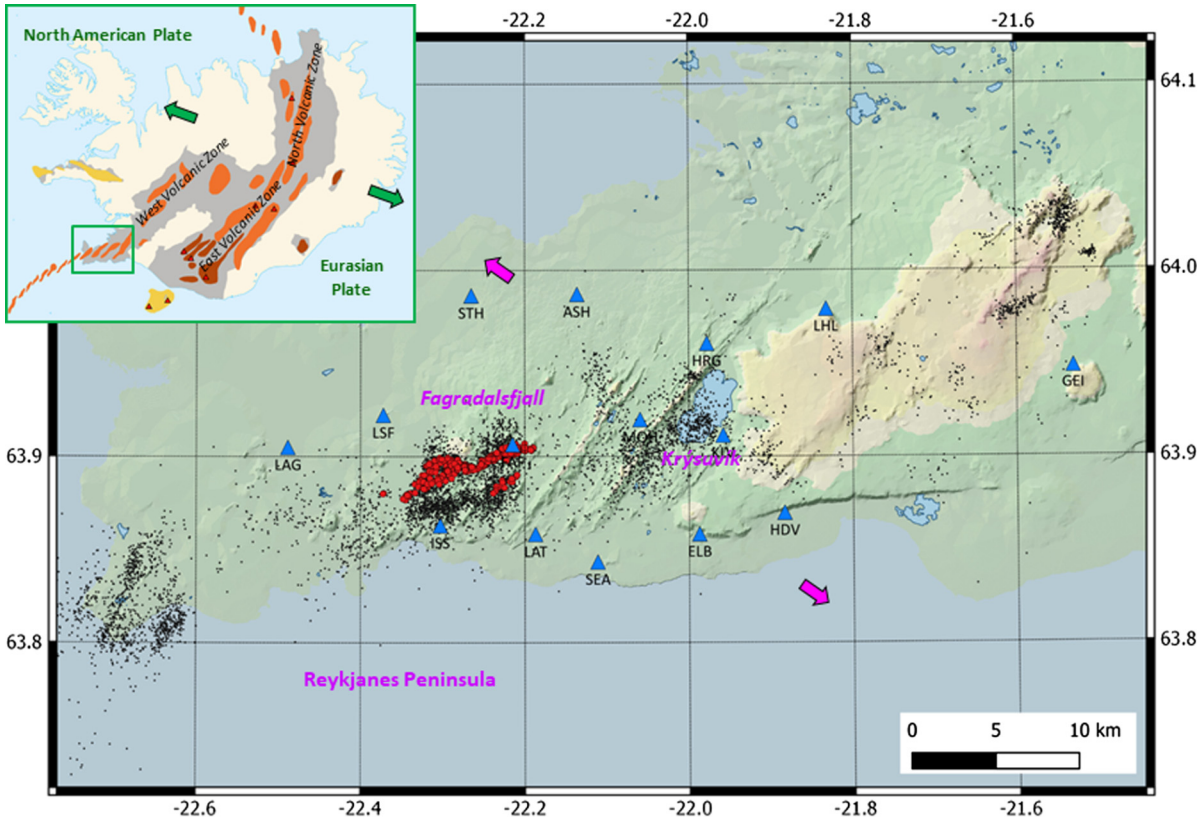

Fig. 1. Topography of the Reykjanes Peninsula in SW Iceland showing the transtensional part of the North Atlantic rift zone onshore. The seismic activity of 2017 swarm detected by the REYKJANET network stations is marked by red dots and is superimposed on the activity between 2013-2019 (black dots) from the SIL catalogue. The REYKJANET seismic stations are indicated by blue triangles. The inset indicates the main tectonics of Iceland with active volcanic zones. The green arrows denote a direction of the Mid-Atlantic extension in Iceland, the violet arrows denote a direction of the extension in the Reykjanes Peninsula. (For interpretation of the colours in the figure(s), the reader is referred to the web version of this article.)

geothermal fields connected to fluid degassing as in the case of the Geysers in the Northern California (Yu et al., 2018, 2019). In tectonic environments, they are often related to the natural fluid degassing (Vavryčuk and Hrubcová, 2017). A dramatic increase of non-DC components is usually associated with volumetric changes in the source and is interpreted as related to the opening of new fracture networks and/or the reactivation of pre-existing critically stressed faults (Cuenot et al., 2006; Šílený et al., 2009; Fischer and Guest, 2011). The observations of fluid-driven earthquakes indicate a connection between the earthquake occurrence and geothermal/magmatic systems as in the Long Valley volcanic region (Templeton and Dreger, 2006). Passarelli et al. (2018) discussed the magmatic or non-magmatic origins of seismic events in the Jailolo volcano, Indonesia, where the swarm earthquakes contained non-DC components with large (∼50%) volumetric changes indicating the fault opening. A large tensile opening of a single fault plane was detected during the volcanic eruption on Miyakejima generating the largest earthquake swarm ever recorded in Japan (Minson et al., 2007) or in long-period events at the Turrialba Volcano, Costa Rica (Eyre et al., 2015).

The reliable non-DC components of moment tensors must be retrieved from local seismic stations with a dense station coverage. In Iceland, studies of non-shear earthquakes are sporadic; data from the Icelandic network of seismic stations SIL are not sufficient for retrieving reliable non-DC components and data from local networks are rare. In this paper, we interpret observations of the REYKJANET network of local seismic stations and investigate source parameters of earthquakes in the 2017 swarm in the Reykjanes Peninsula in SW Iceland. We study not only the foci migration of the earthquakes but also moment tensors and their non-DC components. Since Vavryčuk (2011b) and Vavryčuk et al. (2017) showed that the CLVD components are highly sensitive to errors of the inversion, we focus on the ISO components that are more stable. In addition, the ISO components are more suitable for interpretations, because they have a clear physical meaning. We study a detailed spatiotemporal pattern of the earthquake swarm complemented by determining focal mechanisms and the ISO components for a large set of earthquakes. Finally, we show how the ISO components can help us with understanding the faulting and related processes during a rifting episode.

2. Tectonic setting and seismicity of the Reykjanes Peninsula

Iceland is situated above the Mid-Atlantic Ridge, which separates the North American and the Eurasian plates and represents the only section of the Mid-Atlantic Ridge exposed above the sea level. Such unique setting is a result of an interaction between two different systems: a divergent plate boundary and a stationary mantle plume (Einarsson, 2008). In response to the presence of a hot spot, the Mid-Atlantic Ridge bends across Iceland from the Reykjanes Ridge in the southwest to the Kolbeinsey Ridge in the north (Fig. 1), which, at present, produces transtensional tectonics and intense volcanism. With the spreading rate of ∼19 mm/yr it forms a slow-spreading ridge, which trends 105°E and 285°W (Einarsson, 2008).

The Reykjanes Peninsula in the southwest Iceland represents an oblique rifting boundary oriented ∼30° from the direction of the absolute plate motion and shows a continuation of the rift onshore with 19 mm/yr in the transform motion and 6.5 mm/yr in the extension at 6 km locking depth (Keiding et al., 2009). It is characterized by a high seismicity, recent volcanism and high-temperature geothermal fields. It forms a transition between the

submarine Reykjanes Ridge to the southwest, the Western Volcanic Zone to the northeast, and the South Iceland Seismic Zone to the east. The seismicity zone trends ~N70-80°E in the central part of the Reykjanes Peninsula, but bends towards the south in the western tip of the peninsula before connecting to the Reykjanes Ridge (Fig. 1). The obliquity of the plate boundary indicates a combination of the left-lateral shear and extension, firstly observed from geodesy (Brander et al., 1976). The superposition and the relative motion of the spreading plate boundary over the mantle plume are manifested by the faults and volcanic systems, typically characterized by a central volcano and a fissure (dike) swarm (Thordarson and Larsen, 2007). The fissure swarms of the volcanic systems are oblique to the boundary with a trend of ~40° and extend a few tens of kilometres into the plates on the either side. The Reykjanes Peninsula hosts a large number of NE-SW trending volcanic fissures, a series of NE-SW striking normal faults and N-S striking right-lateral strike-slip faults crosscutting the normal faults (Clifton and Kattenhorn, 2006) forming a thin crust of active Holocene volcanic systems with the youngest rocks along the axis of the Reykjanes Volcanic Belt. The fissures and faults are made up of right-stepping volcano-tectonic segments, where both earthquake swarms and mainshock-aftershock sequences are observed with a systematic change from primarily earthquake swarms in the west to mainshock-aftershock sequences in the east (Keiding et al., 2009). The fissures and faults are grouped into clusters and are usually named after the geothermal areas that occur in their central part (Einarsson, 2008; Einarsson et al., 2018).

The seismicity at the Reykjanes Peninsula is high and episodic with the activity occurring every 30 years (Björnsson et al., 2018; Einarsson, 1991). Recent active periods were at the beginning of the 20th century, during 1929-1935, 1967-1973, 1997-2006, and continue to present. The largest earthquakes in the latest episodes ($M_L < 6$) are known to have been associated with the strike-slip faulting (Einarsson, 1991; Keiding et al., 2009). The seismic energy is released in the form of earthquake swarms, sometimes as a mainshock-aftershock activity and is largely confined to the upper few kilometres of the oceanic layer related to a large number of faults and fissures at depths from 2 km to 6 km. However, some events may be as deep as 13 km (Keiding et al., 2009). The individual swarms last typically a few days, then build-up and terminate gradually.

In the central part of the Reykjanes Peninsula, the earthquakes are located in two areas, Fagradalsfjall and Krýsuvík, forming spatially dense clusters characterized by a pronounced swarm activity superimposed on a relatively low background (Keiding et al., 2009). Earthquake swarms are very common in this region, mostly of tectonic origin, with the latest ones in May 2009 (strongest shock with M_L of 4.7), in December 2019 (M_L of 3.7), or in July 2020 (M_L of 5). Due to the unique geological setting, the tectonic and magmatic origins of earthquakes are closely related, also because of the magma rising through the crust and inducing the earthquakes along its way upwards.

3. Data

3.1. Earthquake swarm in 2017

In this study, we interpret waveforms of the earthquakes occurring during the 2017 swarm recorded at the REYKJANET network. This network consists of 15 local seismic stations (Fig. 1) equipped with the Guralp CMG-3ESPC broadband seismometers and the Nanometrics Centaur data loggers enabling continuous recordings with 250 Hz sampling rate (Horálek, 2013). We interpret waveforms recorded at stations deployed in the epicentral distance up to 20 km from the swarm, where automated detections of the P- and S-wave onsets were refined by manual picking to properly identify multiple earthquakes frequently occurred during the swarm activity.

The 2017 swarm occurred at the turn of July and August 2017 and was located SW of Krýsuvík in the Fagradalsfjall volcano-tectonic fissure segment (Fig. 1) with the last eruption ~6,000 yr ago. The swarm formed a spatially dense cluster, where the most energy was released within the first three days (26-28 July 2017), though some weak activity with a few lower-magnitude shocks also occurred in August 2017 (Fig. 2). The strongest shock was of $M_L = 3.7$ and the seismic activity consisted of more than 2,000 earthquakes with $M_L > 0$.

3.2. Locations of the 2017 earthquakes

The events formed a 9-km-long cluster of the WSW-ENE strike (67°) in a depth range from 2 to 6 km (Fig. 2 and Supplementary Movie S1) determined by the relative double-difference location method (Waldhauser and Ellsworth, 2000). This method utilised differential traveltimes derived from the cross-correlation and resulted in the relative location accuracy of about 100 m. The magnitude separation between the largest and the other earthquakes was ~0.5 which points to a hybrid activity between the earthquake swarm and the mainshock-aftershock sequence, similarly as reported by Keiding et al. (2009) for this area.

The fault system of the 2017 swarm has an overall strike of ~67° (Figs. 1 and 2, and Supplementary Movie S1), but detailed double-difference locations and a further analysis of focal mechanisms suggest individual fault segments with slightly different orientations in strike and dip angles. The spatiotemporal distribution of earthquakes shows a general migration of the activity from the ENE to the WSW along two steeply dipping echelon fault segments with a dip of ~85° in the east and a dip of ~70° in the west. In the central part of the fault zone, a gap of missing foci is visible at depths 3-6 km (Fig. 2d, and Supplementary Movie S1) suggesting either a barrier between eastern and western parts or a ductile deeper-seated magmatic intrusion. The location of the small sub-cluster of events southerly of the main fault 2017 zone (Figs. 1 and 2) coincides with the subsequent activity of the 2019 swarm.

3.3. Determination of focal mechanisms and moment tensors

The focal mechanisms and seismic moment tensors of the 2017 swarm earthquakes were calculated from amplitudes of the direct P waves (Fig. 3) acquired in an automated way. To get reliable solutions, we analysed earthquakes with magnitude $M_L > 1$, which resulted in processing of 389 double-difference located events. The most of events (87%) had the magnitude $M_L < 2.3$ with the peak at $M_L = 1.6$. The moment tensors (MTs) were calculated with the ray-theoretical Green's functions including geometrical spreading and conversion coefficients at the free surface (Červený, 2001) and using the generalized linear inversion (Vavryčuk, 2011a). The velocity model was a smooth version of the layered model of Stefánsson et al. (1993) used for the locations (see Table 1); the Q factor was estimated in accordance with Menke et al. (1995) for SW Iceland. The P-wave amplitudes were measured at the vertical component of the velocity records observed at stations with the epicentral distance up to 20 km. The horizontal components were not used being noisier and thus withholding any new information for the inversion. The prevailing frequency of the P waves were detected between 8-10 Hz (Fig. 4); the P-wave Q factor was related to the reference frequency of 10 Hz, the predominant frequency of the analysed P waves.

The amplitudes of the direct P waves needed in the MT inversion were determined with the principal component analysis according to Leaney (2014) and Vavryčuk et al. (2017). The method

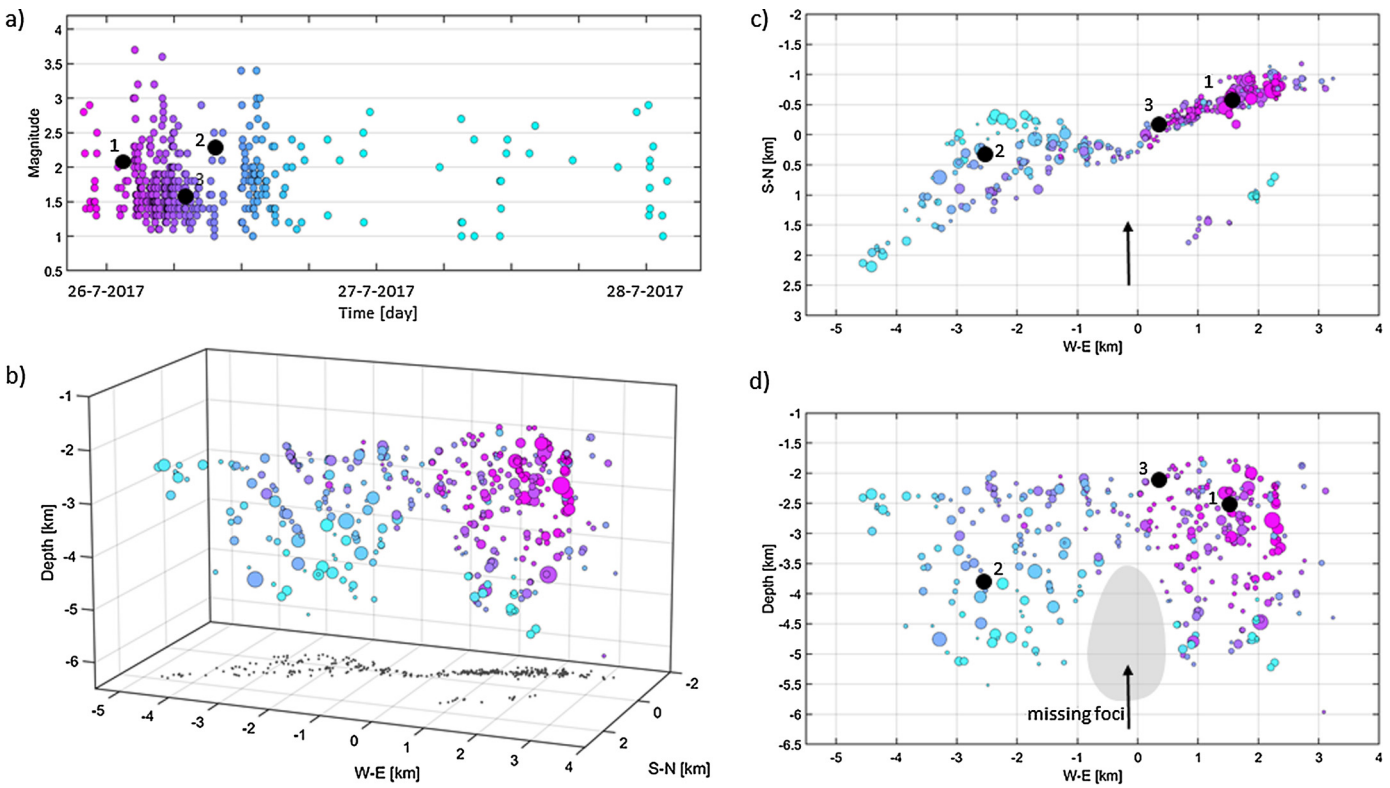

Fig. 2. The spatiotemporal evolution of the 2017 swarm in the Fagradalsfjall shield volcano, Reykjanes Peninsula from double-difference locations ($M_L > 1$). The colour-coding is proportional to the origin time (from magenta to cyan); the event magnitude is indicated by the circle size. (a) The magnitude-time plot; (b) the 3D view of foci; (c) the map view of foci; (d) the vertical-section view of foci. Notice the area of a missing activity marked by shaded area and the black arrow, which indicates a possible magmatic dike. The black dots mark foci of earthquakes with the waveforms shown in Fig. 3.

Table 1
Seismic velocity model.

Depth (km)	Vp top (km/s)	Q_P
0	3.53	75
1	4.47	100
2	5.16	125
3	5.60	150
4	5.96	175
5	6.22	200
6	6.50	200
7	6.60	225
8	6.66	225
9	6.73	225
15	7.00	300
20	7.20	350
30	7.40	450

The P-wave Q factor is related to the reference frequency of 10 Hz, the predominant frequency of the analysed P waves.

is based on the determination of the common wavelet from the observed P waveforms, which were cross-correlated, aligned and windowed to extract the direct P wave (Fig. 3). A subsequent cross-correlation of the common wavelet with the direct P wave gave the so-called principal component amplitude (PCA) at each station, which served as the effective amplitude (including polarity) used in the amplitude inversion for the full MTs with no *a priori* constraint. The approach is fully automated being less sensitive to noise and thus more accurate and robust than the manually picked amplitudes. Since the waveforms are cross-correlated before determining the PCAs, the MT inversion is also less sensitive to mislocations of the earthquakes and to an inaccurate velocity model including a roughly estimated Q factor in this heterogeneous magmatically active region.

To eliminate the effect of a varying predominant frequency of the P waves due to the magnitude of the earthquakes, the PCA MT inversion was applied to data filtered in several frequency bands (Yu et al., 2019). The analysed velocity records were filtered by a series of bandpass Butterworth filters with the low corner frequency alternatively of 1 or 1.5 Hz, and with the high corner frequency alternatively of 8, 10, 12 and 14 Hz (Fig. 3). Subsequently, the sets of the PCAs corresponding to the individual frequency bands were used in the MT inversions. The optimum frequency band finally applied was the one that produced the MT with the lowest normalized root-mean-squares (RMS) of differences between the theoretical and observed amplitudes at all stations for each event (Vavryčuk et al., 2017, their equation (9)).

Moreover, the stability of the MT inversion was assessed by numerical tests. To simulate various path and site effects and other unaccounted factors unmodelled in the Green's functions, the input PCAs were contaminated by random noise and inverted repeatedly for the MTs. The level of noise was 25% of the P-wave amplitude at each trace and the probability distribution of random noise was flat. We used 100 realizations of noise to obtain statistically significant results. The scatter of the MTs determined from noisy data served for estimating the accuracy of the focal mechanisms as well as of the ISO components, and subsequently for selecting the most reliable solutions. We also tested the reference frequency of the P-wave Q factor and finally related it to the reference frequency of 10 Hz, which is the predominant frequency of the analysed P waves.

4. Results

4.1. Selection of reliable moment tensors

The retrieved MTs of the 389 analysed earthquakes were differently accurate, which was indicated by: (1) the number of stations

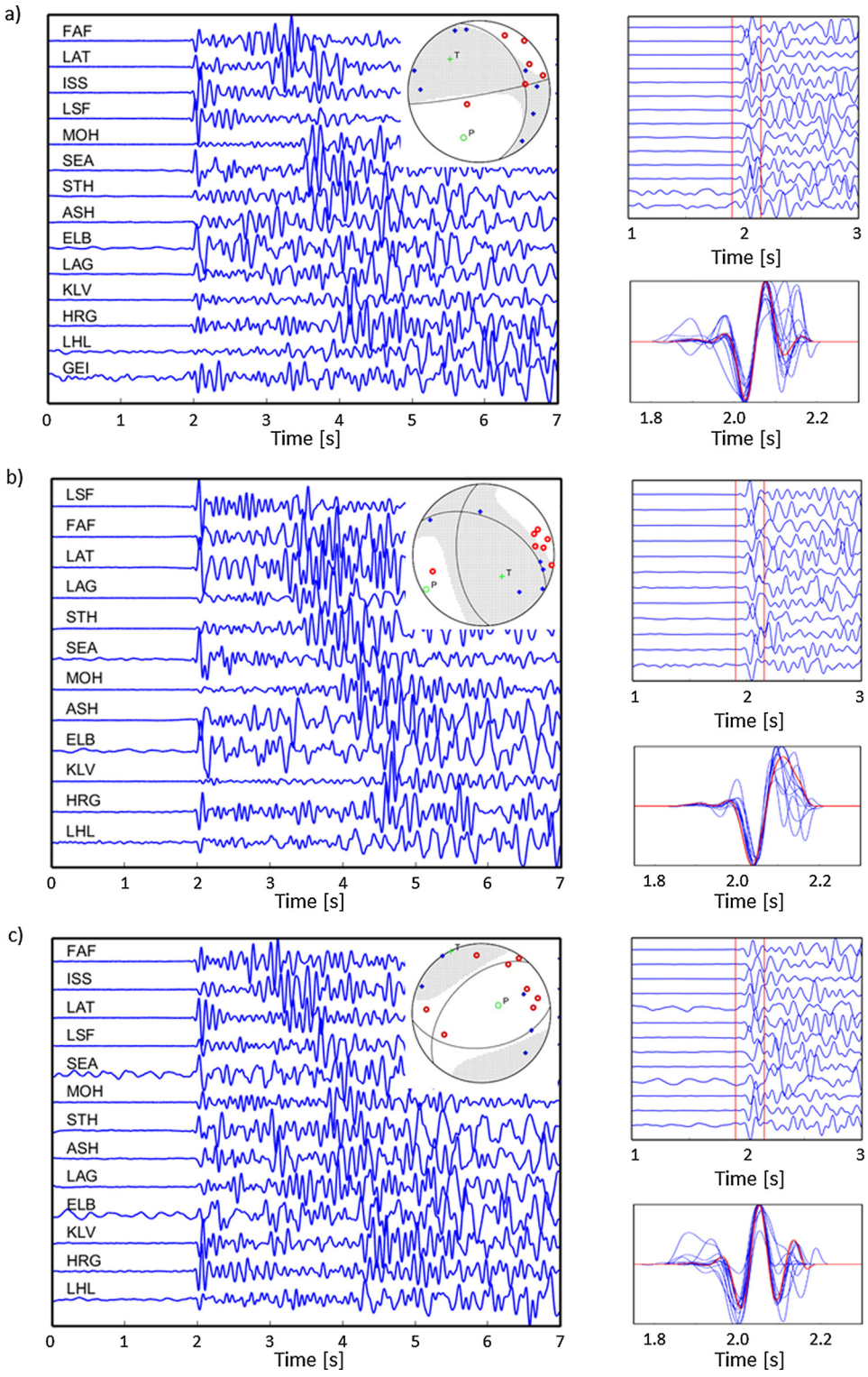

Fig. 3. Vertical waveforms of three earthquakes on 26th July 2017 recorded by REYKJANET stations. (a) Event 816218, mechanism 1, depth 2.5 km, $M_L = 2.1$; (b) event 819193, mechanism 2, depth 3.8 km, $M_L = 2.3$; (c) event 820006, mechanism 3, depth 2.1 km, $M_L = 1.6$. Waveforms are aligned according to P-wave onsets and filtered by the 1.5-14 Hz bandpass to remove low- and high-frequency noise. In each plot, the left subpanels show the whole velocity records; the upper right subpanels show the cross-correlated waveforms; the lower right subpanels show superposition of the cross-correlated waveforms (blue) and the first principal component representing the common wavelet from the PCA analysis (red); the insets in the left subpanel show focal mechanisms and positions of stations on the focal sphere (red circles – negative P-wave polarities, blue plus signs – positive P-wave polarities). The locations of events are marked in Fig. 2.

used for the inversion; (2) the RMS of the retrieved optimum MT solutions; (3) the mean deviations of the pressure and tension axes (P and T axes) between the MTs inverted using noise-free and noisy data; and (4) the standard errors of the percentage of the ISO component. To eliminate unreliable solutions, we selected 251 the most accurate MTs by applying the following quality criteria: (1) the number of stations recording the earthquakes higher or equal to 10; (2) the RMS lower than 0.3; (3) the mean deviation of the P/T axes lower that 12°; and (4) the standard deviation of the ISO percentage lower than 12%. In this way, we eliminated 'problem-

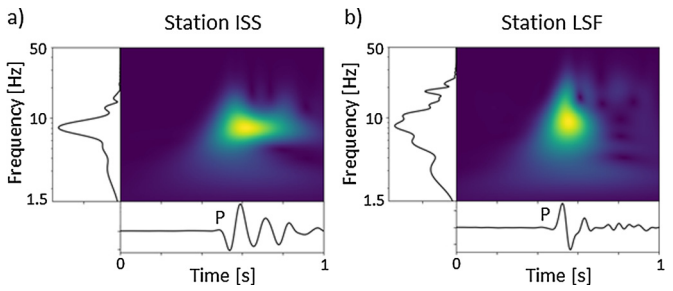

Fig. 4. Spectrograms of the vertical P-wave recordings of two 2017 earthquakes with different magnitudes and focal mechanisms recorded at two REYKJANET stations. (a) Station ISS, event 816218, $M_L = 2.1$, depth 2.5 km; (b) Station LFS, event 820020, $M_L = 1.5$, depth 3.1 km. The corner frequency of the high-pass filter was 1.5 Hz. Note the prevailing frequency of the P waves between 8-10 Hz. For station locations see Fig. 1.

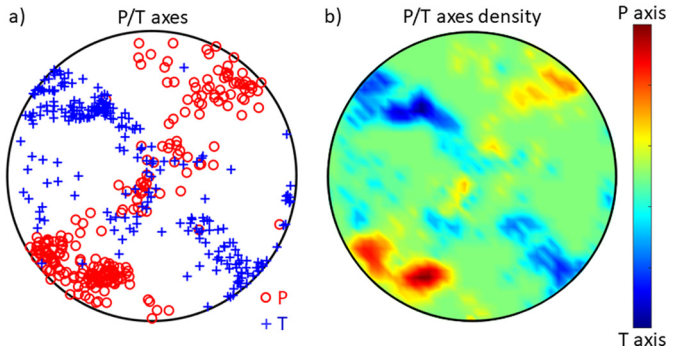

Fig. 5. Composite plots of the pressure and tension axes (P/T axes) of 251 selected MT solutions of the 2017 swarm earthquakes. (a) The P/T axes of individual events; (b) the density plot of the P/T axes. The P/T axes are calculated from the DC part of the MTs. Note two clusters of the T axes in the NW and SE directions (∼310° and ∼140°) corresponding to the extensional setting of the rift zone.

atic' events with unfavourable station coverage or with amplitudes significantly distorted by unmodelled effects.

The resulting fault plane solutions are depicted in the composite plot of the P/T axes of the 251 selected solutions (Fig. 5). The T axes form two condense clusters in the NW-SE direction (∼140°) corresponding to the extensional setting of the main rift zone in the Reykjanes Peninsula. Compared to the T axes, the P axes form two pronounced sub-horizontal clusters in the SW and a less compact sub-horizontal cluster in the NE direction. A portion of events displays the P/T axes in the near-vertical directions representing reverse/normal faulting.

4.2. Classification of moment tensors

As seen from Fig. 5, the clusters of the P/T axes of the 251 reliable solutions do not overlap and are well separated except for the near-vertical directions, where the P and T axes are mixed. The pattern of the clustered P/T axes suggests the presence of some typical or representative focal mechanisms in the dataset. Finding these focal mechanism types can help in identifying the basic fracturing modes and different fault segments activated in the focal zone.

The representative MTs can be determined by applying the cluster analysis with the *k*-means clustering algorithm (Jain, 2010), where each cluster of MTs is defined by its centroid. The positions of the centroids are found by minimizing the sum of distances of all full MTs (Willemann, 1993; Cesca et al., 2014). The cosine distance measures the differences between individual MTs in the clustering procedure (Vavryčuk et al., 2017, their equations (10)-(11)). The only parameter controlling clustering is the number of clusters. After tests we found that the classification of MTs into three clusters is optimum. Such a classification appeared sufficiently simple, but still revealed distinct stable basic types of MTs in the data. Classifying data into more clusters was not helpful and revealed unnecessary details, when some of the representative focal mechanisms were similar. Obviously, interpretations in future studies could profit from a more detailed clustering.

The final classification of the moment tensors revealed three distinct types of representative focal mechanisms (Fig. 6) corresponding to the activation of three different fault segments. The majority of events displayed the first-type mechanism occurring along the fault oriented nearly in the WSW-ENE direction with a strike of 83°. It was characterized by the oblique left-lateral strike slip with a weak normal component located predominantly in the eastern fault segment (Fig. 6, red colour). These events initiated the swarm activity. The second type showed the strike-slip mechanism with a shear motion either in the N-S direction with a strike of 166° or a shear motion in about E-W direction (strike of 107°). This system was less active occupying mainly the western fault segment (Fig. 6, blue colour) and appearing in the final stages of the swarm activity. The third type occurred predominantly in the central part of the fault above the gap of missing foci with the normal mechanism and the SW-NE strike of 43° (Fig. 6, green colour) and the T axis of 300°. This system corresponded to the extensional setting of the rift environment with the azimuth of 130°. Its spatiotemporal evolution suggests that it is related to the interconnection of the eastern and western fault segments. The parameters of representative clusters are summarized in Table 2.

4.3. Non-double-couple components

In order to further understand the properties of fracturing during the 2017 swarm, we studied the ISO component of the retrieved MTs. The ISO component is closely related to volumetric changes in the earthquake source and it can inform us about the mode of fracturing. The zero ISO characterizes shear fracturing; the positive ISO is produced by opening of tensile cracks, and the negative ISO is produced by crack closures (Frohlich, 1994; Julian et al., 1998; Vavryčuk, 2011b, 2015; Vavryčuk et al., 2017). Hence, the ISO component can trace the occurrence of shear/tensile/compressive fracturing and map stress changes and fluid flow in the focal area (Vavryčuk et al., 2021).

The non-DC components of MTs of the 2017 swarm revealed significant ISO components in a range from −25% to 30% (Fig. 7) with different spatial distributions along the fault. They were prevailingly close to zero in the eastern fault segment for events that initiated the faulting, and they were positive in the western fault segment for events that terminated the faulting. The events in the central part of the fault around the gap of missing foci exhibited predominantly negative ISO components.

The spatiotemporal character of the ISO components coincides with systematic trends in the mechanism types. The ISO is close to zero for events of the first-type mechanism (Fig. 6, red colour), it is positive for events of the second-type mechanism (Fig. 6, blue colour), and finally it is negative for events of the third-type mechanism (Fig. 6, green colour). The systematic trends show that the ISO component is an important factor in differentiating individual fracture modes and stress regimes along the fault.

4.4. Errors and the uncertainty analysis

The clustering of MTs and the systematic trends in the ISO components along the fault are striking and invoke a question, whether they really reflect true fracture processes or they are just numerical errors of the MT inversion, for example, due to varying station

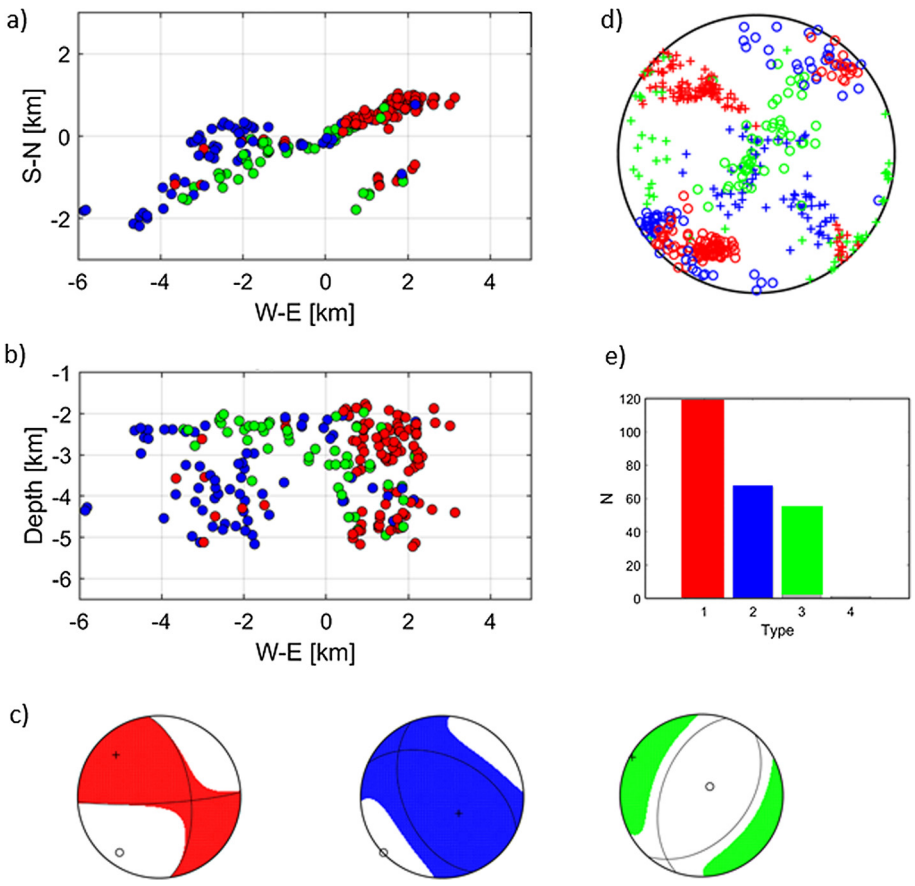

Fig. 6. The three-cluster analysis of moment tensors. (a) The map view; (b) the vertical-section view; (c) the typical focal mechanisms for each cluster; (d) the P/T axes of individual events; (e) the distribution of events in individual clusters. The colour coding is according to the three retrieved clusters. Note the prevailing occurrence of the first-type events (red) in the eastern fault segment, the second-type events (blue) in the western fault segment, and the third-type events (green) in the central part of the fault.

Table 2
Double-couple and isotropic components of the representative moment tensors.

Cluster	Strike1 (°)	Dip1 (°)	Rake1 (°)	Strike2 (°)	Dip2 (°)	Rake2 (°)	DC (%)	CLVD (%)	ISO (%)
1	341.9	40.7	158.2	88.7	76.0	51.3	65.8	−26.9	7.3
2	274.1	79.0	15.4	181.1	74.8	168.6	51.4	−30.2	18.4
3	34.1	42.3	−77.8	197.8	48.9	−100.9	55.1	−22.1	−22.8

The percentages of double-couple and isotropic components were calculated with the equations (6)-(10) of Vavryčuk (2015).

coverage along the fault or an inaccurate velocity model. Therefore, we performed a series of additional numerical tests, which confirmed the true nature of the P/T and ISO patterns in the data.

(1) We quantified the errors of the P/T axes and ISO exercising 100 repeated MT inversions of data contaminated by random noise (Fig. 8). In this way, we simulated various path and site effects, unmodelled in the Green's functions. The analysis showed that the P and T standard errors were less than 2° and 5°, respectively, and the standard errors in the ISO percentage was less than 3%. Such errors could not affect MT clustering as well as the overall pattern of the ISO components, because the observed ISO attained much higher percentages (Fig. 7).

(2) We imposed even stricter quality criteria for selecting the most accurate MTs and checked if the observed clustering and the ISO pattern persist or not. We found that the focal mechanism types can slightly vary (up to 10° in strike, dip or rake angles), but the classification into three basic types of focal mechanisms (e.g., shear strike-slip events, compressive normal faulting events, and extensive oblique strike-slip events) was stable.

(3) To assess the effects of the inaccurate velocity model and inaccurate event locations, we calculated the MTs for systematically biased event depths. We gradually varied the depth of all events in the range of ± 500 m with a step of 100 m. We found that the sum of the RMS in the MT inversion for all events slightly changed with depth and that the MTs with foci shallower by 500 m yielded an optimum RMS value. In this way, the inversion helped to improve the velocity model. However, no systematic effect on clustering and on the ISO pattern was visible.

(4) To estimate errors in the MTs due to inaccurate attenuation of the structure, we considered several differently attenuating models in the MT inversion including a model with no attenuation. We also tested the reference frequency of the P-wave Q factor. The tests showed that the Q factor could strongly affect the scalar moments of the MTs, but the P/T axes and the ISO components were mostly unaffected.

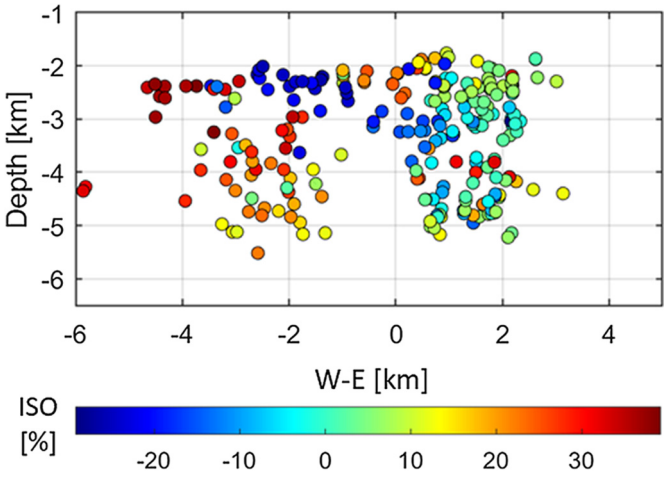

Fig. 7. The ISO components of the 2017 swarm earthquakes along the fault. The circles show the locations of events colour-coded according to the ISO percentage. Note the prevailing low ISO in the eastern fault segment, the positive ISO in the western fault segment, and the predominantly negative ISO in the central part of the fault.

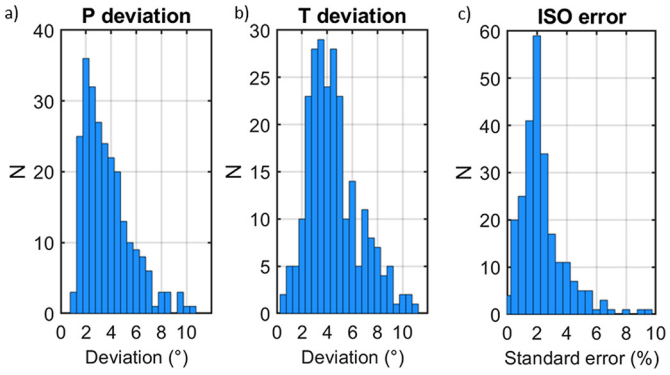

Fig. 8. The histograms of mean deviations of the P/T axes (a-b) and the histogram of the standard errors of the ISO percentage (c) for the 251 selected events of the 2017 swarm. For each event, the mean P/T deviations and the standard errors of the ISO were calculated from 100 solutions of MTs inverted using the P-wave amplitudes contaminated by random noise.

5. Discussion

The MTs of the 2017 swarm earthquakes at the Reykjanes Peninsula contain significant ISO components indicating volumetric changes in the focal zone. Non-DC changes in volcano-tectonic environments are also reported by other authors (Nettles and Ekström, 1998; Oliva et al., 2019) and are supported by analogue experiments and modelling. Trippanera et al. (2015) simulated progressive dike intrusions and growth of a dike swarm and found contraction structures with shallower intrusions promoting normal faults propagating downwards. They compared their results with observations in Krafla, Iceland (Brandsdóttir et al., 1997), Dabbahu, Afar (Ebinger et al., 2010), or Barðarbunga, Iceland (Sigmundsson et al., 2014) and highlighted the overall similar deformation patterns. Normal faults with collapsed structures were retrieved by digital image correlation techniques aimed at the volcanic spreading and the fault interaction influenced by rift zone intrusions (Le Corvec and Walter, 2009). Tentler and Temperley (2007) modelled normal faulting in connection to fissure swarms in Iceland and concluded that magmatic fissures have vertical feeders and their inflation/deflation during an eruptive cycle causes subsidence.

The ISO components of the 2017 swarm displayed a systematic spatiotemporal distribution related to the evolution of faulting at different fault segments. The 2017 activity started in the east with strike slips and close to zero volumetric components (Fig. 9, red colour). Since the strike of the mechanisms coincided with the strike of the transform rift (∼75-80°), these earthquakes should be related to transform faulting of the North Atlantic Rift environment.

The strike-slip events were followed by the normal SW-NE faulting prevailingly in the central part of the fault. The events with negative ISO components are mostly concentrated above the aseismic gap (Fig. 9, green colour) and indicate subsidence and collapses due to the overall extensional regime in the crust. This is supported by the following facts: (1) the strike of the representative mechanism is ∼43° which is close to the strike of magmatic fissures with a trend of ∼40°; and (2) the tension axis of the representative mechanism was ∼300° which matched the spreading direction of the Iceland rift environment slightly rotated due to transtensional tectonics in the Reykjanes Peninsula.

Contrary to the positive components, the negative volumetric components are usually related to crack closures resulting in subsidence. The subsidence at divergent plate boundaries is attributed to collapses of the roof of the shallow magma chambers associated with volcanism (Shuler and Ekström, 2009) and lateral migration of magma (Einarsson and Brandsdóttir, 1980). Nettles and Ekström (1998) discussed highly non-DC focal mechanisms of several events related to the inflation of a shallow magma chamber in Iceland. The dike intrusion events sourced from a shallow crustal magma reservoir near the centre of the rift segments was also reported for Krafla, Iceland (Brandsdóttir et al., 1997); a volcanic rift subsidence in Krafla was discussed by Rubin (1992).

The connection of normal faulting with the magmatic activity was also suggested by Clifton and Kattenhorn (2006) from GPS data. The explanation implicates that during a rifting episode magma from a shallow chamber was injected into the volcanic fissures similarly as discussed by Tentler and Temperley (2007) and the inflation and deflation of a fissure feeder caused normal faulting, subsidence and negative volumetric components. This required the presence of a magma reservoir with a significant vertical component and thus a magma chamber beneath the rift. Though not foreseen in the case of slow-spreading ridges, accumulated melt beneath the Reykjanes Ridge axis of the Mid-Atlantic Rift was revealed from the multi-component geophysical experiment (Sinha et al., 1997). Also the reflection survey (Singh et al., 2006) detected the presence of a crustal magma body beneath the slow-spreading segment of the Mid-Atlantic Ridge at depth of 3 km beneath the sea floor.

Terminating events of the 2017 swarm were located in the west, with oblique strike-slips (Fig. 9, blue colour), detected also by Clifton and Kattenhorn (2006) or modelled by Clifton and Schlische (2003). They can be attributed to a complex (bookshelf) faulting (Einarsson, 2008) related to the transcurrent movement at the transform fault. The W-E oriented strike-slips corresponded to the main activated transform fault, witnessed also from the strike of foci locations at this part of the fault (Fig. 9, and Supplementary Movie S1). On the other hand, the transcurrent component of the movement was accommodated by strike-slip faulting on the fault that was transverse to the plate boundary segment witnessing the transient nature of the segments.

Volumetrically, these events exhibited positive volumetric components pointing to tensile opening due to the high pore pressure of fluids propagating through the fluid-filled fractures. The brittle crust, probably cracked during the preceding stages of fracturing, enabled the accumulated fluids to flow and trigger the earthquakes on favourably oriented faults as discussed also by Passarelli et al. (2018). This is also supported by results of Gilbert and Lane (2008), who suggested that volatiles and fluid flow within the active volcanic conduit support the magma motion at active volcanoes. This idea is promoted by the presence of the Fagradalsfjall shield vol-

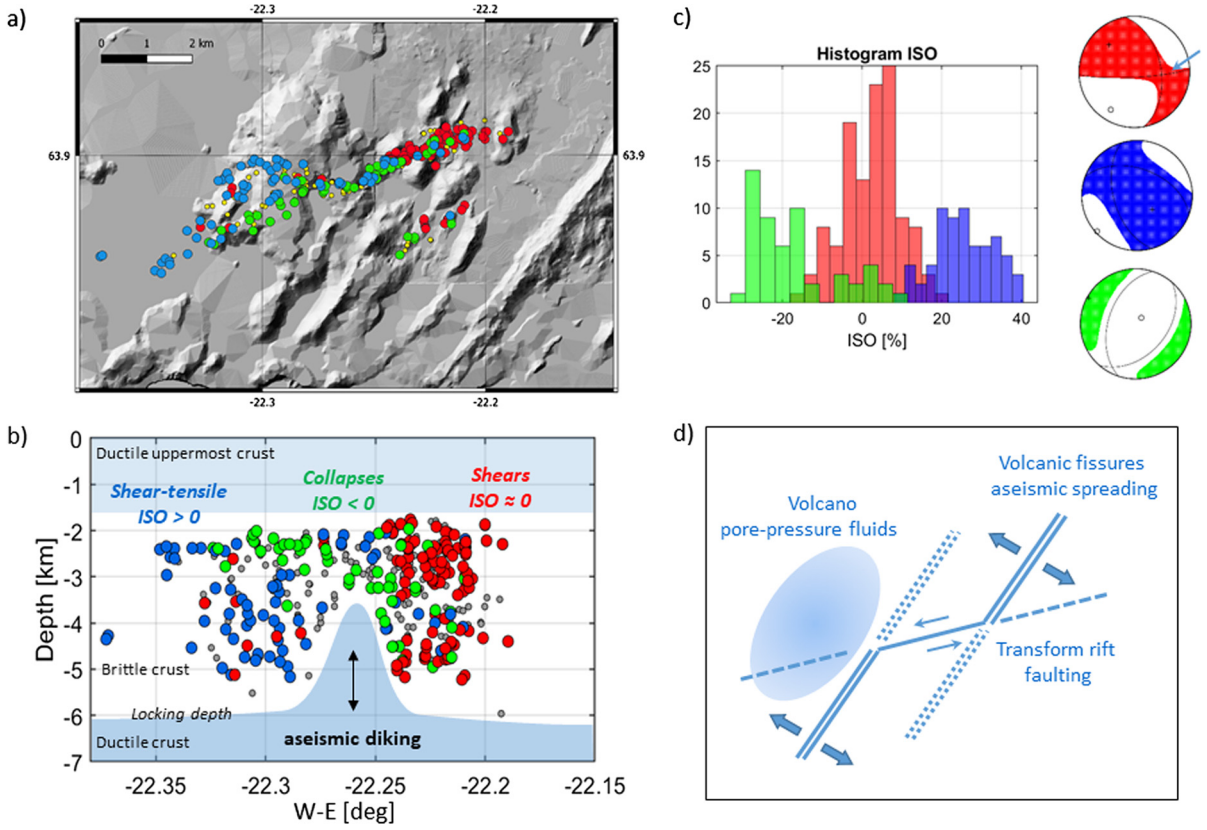

Fig. 9. The interpretation of moment tensors of the 2017 swarm. (a) The map view of the event-type distribution superimposed on the Fagradalsfjall topography; (b) the vertical-section view of the event-type distribution with a schematic interpretation of three different tectonic regimes superimposed on idealized brittle/ductile crustal segments; (c) the distribution of the ISO components according to clusters with the representative focal mechanisms and the blue arrow indicating transform shearing; d) the schematic map view of the rift zone with the transform and extensional tectonics; the arrows indicate a relative displacement across the dislocation surface. The colour coding of events indicates their mechanism types; the yellow and grey dots in (a) and (b) plots, respectively, mark the events with $M_L > 1$ (see Fig. 2) eliminated from the MT clustering. Note the positive ISO for events with the second-type mechanism (blue), close to the zero ISO for events with the first-type mechanism (red), and the negative ISO for events with the third-type mechanism (green).

cano (last eruption ~6,000 yr ago), solidified in the uppermost crust, which can trap a high amount of volatiles from volcanic conduits being released when fractured during the 2017 earthquake swarm. The large amount of volatiles for such activity is also supported by the Krýsuvík high temperature geothermal area nearby. Hersir et al. (2020) showed an indication of a conductive body in Krýsuvík and suggested that the inflation/deflation periods are linked to the gas flux.

Note that a small sub-cluster of events in the SE of the main 2017 fault zone (Figs. 1 and 8) indicates the initiation or reactivation of another fault segment in the Reykjanes Peninsula, which was mostly active during the subsequent activity of the 2019 swarm.

6. Conclusions

The double-difference locations, focal mechanisms and systematic trends of the non-DC volumetric components revealed three segments of the activated fault suggesting continuous interactions between tectonic and magmatic processes. They are related to inflation/deflation of a vertical magmatic dike and comprise: (1) shearing at the strike-slip transform fault with left-lateral motion complemented by (2) collapses at normal faulting with negative volumetric components due to magma/fluid escape, and (3) shear-tensile opening at oblique strike-slip faulting with positive volumetric components connected to the flow of trapped overpressurized fluids at fractures in the Fagradalsfjall shield volcano (Fig. 9).

The three regimes of the complex spatiotemporal volcano-tectonic evolution of divergent plate movements are documented at the transtensional Reykjanes plate boundary. (1) The extensional component is accommodated by aseismic spreading in the volcanic fissures trending SW-NE connected with diking. Brittle faulting related to the magmatic activity is associated with collapses and normal faulting above or close to the dikes with the same strike as the volcanic fissures. (2) The transform component is accommodated by the WSW-ENE trending strike-slip faults associated with the most active faulting along the transform boundary. In minority, they are accompanied by the north-south trending strike-slips related to a complex (bookshelf) faulting of a highly oblique divergent boundary. (3) The positive volumetric components appear at the final stages of the faulting. They are probably connected with over-pressurized fluids, which migrate through the fractures on favourably oriented transtensional faults corresponding to the transform setting of the Reykjanes Peninsula rift environment.

To conclude, the 2017 Reykjanes Peninsula swarm recorded by a dense network of local broadband seismic stations provided a unique and very detailed insight to the emplacement of magma in a divergent slow-rift setting. The key role in the interpretation was achieved by accurately determined seismic moment tensors and, particularly, their non-DC volumetric components. The systematic trends in these components proved their importance in differentiating individual stress regimes and faulting processes, and in mapping the fluid flow in the focal zone. The identification of three regimes of complex volcano-tectonic evolution in divergent plate movement proved an enormous capability of the non-DC volumetric components to map tectonic processes in such settings.

CRediT authorship contribution statement

Pavla Hrubcová: Conceptualization, Methodology, Investigation, Writing, Visualization. **Jana Doubravová:** Data acquisition and pre-processing. **Václav Vavryčuk:** Methodology, Software, Editing, Funding acquisition.

Declaration of competing interest

The authors declare that they have no known competing financial interests or personal relationships that could have appeared to influence the work reported in this paper.

Acknowledgements

This work was supported by the Czech Science Foundation, grants 18-05053S and 19-06422S. The data acquisition was supported by the project of the large research infrastructure CzechGeo, No. LM2010008. The authors are grateful to Josef Horálek for providing with the data. The authors also thank Hans Thybo (Editor) and two anonymous reviewers for their detailed comments and suggestions that helped to improve the manuscript.

Appendix A. Supplementary material

Supplementary material related to this article can be found online at https://doi.org/10.1016/j.epsl.2021.116875.

References

Acocella, V., Neri, M., 2009. Dike propagation in volcanic edifices: overview and possible developments. Tectonophysics 471 (1–2), 67–77. https://doi.org/10.1016/j.tecto.2008.10.002.

Björnsson, S., Einarsson, P., Tulinius, H., Hjartardóttir, Á.R., 2018. Seismicity of the Reykjanes Peninsula 1971-1976. J. Volcanol. Geotherm. Res. 391, 106369. https://doi.org/10.1016/j.jvolgeores.2018.04.026.

Brander, J.L., Mason, R.G., Calvert, R.W., 1976. Precise distance measurements in Iceland. Tectonophysics 31, 193–206.

Brandsdóttir, B., Menke, W., Einarsson, P., White, R.S., Staples, R.K., 1997. Færoe-Iceland ridge experiment 2. Crustal structure of the Krafla central volcano. J. Geophys. Res. 102, 7867–7886.

Cesca, S., Sen, A.T., Dahm, T., 2014. Seismicity monitoring by cluster analysis of moment tensors. Geophys. J. Int. 196, 1813–1826.

Clifton, A.E., Kattenhorn, S.A., 2006. Structural architecture of a highly oblique divergent plate boundary segment. Tectonophysics 419, 27–40.

Clifton, A.E., Schlische, R.W., 2003. Fracture populations on the Reykjanes Peninsula, Iceland: comparison with experimental clay models of oblique rifting. J. Geophys. Res. 108 (B2), 2074. https://doi.org/10.1029/2001JB000635.

Cuenot, N., Charléty, J., Dorbath, L., Haessler, H., 2006. Faulting mechanisms and stress regime at the European HDR site of Soultz-sous-Forêts, France. Geothermics 35 (5–6), 561–575. https://doi.org/10.1016/j.geothermics.2006.11.007.

Červený, V., 2001. Seismic Ray Theory. Cambridge University Press, Cambridge.

Dreger, D.S., Tkalcic, H., Johnston, M., 2000. Dilatational processes accompanying earthquakes in the Long Valley Caldera. Science 288, 122–125.

Ebinger, C., Ayele, A., Keir, D., Rowland, J., Yirgu, G., Wright, T., Belachew, M., Hamling, I., 2010. Length and timescales of rift faulting and magma intrusion: the Afar rifting cycle from 2005 to present. Annu. Rev. Earth Planet. Sci. 38 (1), 439–466. https://doi.org/10.1146/annurev-earth-040809-152333.

Einarsson, P., 1991. Earthquakes and present-day tectonism in Iceland. Tectonophysics 189, 261–279.

Einarsson, P., 2008. Plate boundaries, rifts and transforms in Iceland. Jokull 58, 35–58.

Einarsson, P., Brandsdóttir, B., 1980. Seismological evidence for lateral magma intrusion during the July 1978 deflation of the Krafla volcano in NE-Iceland. J. Geophys. 47, 160–165.

Einarsson, P., Hjartardóttir, Á.R., Imsland, P., Hreinsdóttir, S., 2018. The structure of seismogenic strike-slip faults in the eastern part of the Reykjanes Peninsula oblique rift, SW Iceland. J. Volcanol. Geotherm. Res. 391, 106372. https://doi.org/10.1016/j.jvolgeores.2018.04.029.

Eyre, T.S., Bean, C.J., De Barros, L., Martini, F., Lokmer, I., Mora, M.M., Pacheco, J.F., Soto, G.J., 2015. A brittle failure model for long-period seismic events recorded at Turrialba Volcano, Costa Rica. J. Geophys. Res., Solid Earth 120, 1452–1472. https://doi.org/10.1002/2014JB011108.

Fischer, T., Guest, A., 2011. Shear and tensile earthquakes caused by fluid injection. Geophys. Res. Lett. 38, L05307. https://doi.org/10.1029/2010GL045447.

Frohlich, C., 1994. Earthquakes with non-double-couple mechanisms. Science 264 (5160), 804–809. https://doi.org/10.1126/science.264.5160.804.

Gilbert, J.S., Lane, S.J., 2008. The consequences of fluid motion in volcanic conduits. In: Lane, S.J., Gilbert, J.S. (Eds.), Fluid Motions in Volcanic Conduits: A Source of Seismic and Acoustic Signals. In: Special Publications, vol. 307. Geological Society, London, pp. 1–10.

Hersir, G.P., Árnason, K., Vilhjálmsson, A.M., Saemundsson, K., Ágústsdóttir, B., Friðleifsson, G.Ó., 2020. Krýsuvík high temperature geothermal area in SW Iceland: geological setting and 3D inversion of magnetotelluric (MT) resistivity data. J. Volcanol. Geotherm. Res. 391, 106500. https://doi.org/10.1016/j.jvolgeores.2018.11.021.

Horálek, J., 2013. Reykjanet. International federation of digital seismograph networks. Dataset/Seismic Network. http://www.fdsn.org/networks/detail/7E_2013/.

Jain, A.K., 2010. Data clustering: 50 years beyond k-means. Pattern Recognit. Lett. 31, 651–666.

Julian, B.R., Pitt, A.M., Foulger, G.R., 1998. Seismic image of a CO_2 reservoir beneath a seismically active volcano. Geophys. J. Int. 133 (1), F7–F10. https://doi.org/10.1046/j.1365-246x.1998.1331540.x.

Keiding, M., Lund, B., Árnadóttir, T., 2009. Earthquakes, stress, and strain along an obliquely divergent plate boundary: Reykjanes Peninsula, southwest Iceland. J. Geophys. Res. 114, B09306. https://doi.org/10.1029/2008JB006253.

Knopoff, L., Randall, M.J., 1970. The compensated linear-vector dipole: a possible mechanism for deep earthquakes. J. Geophys. Res. 75 (26), 4957–4963. https://doi.org/10.1029/jb075i026p04957.

Le Corvec, N., Walter, T.R., 2009. Volcano spreading and fault interaction influenced by rift zone intrusions: insights from analogue experiments analyzed with digital image correlation technique. J. Volcanol. Geotherm. Res. 183 (3–4), 170–182. https://doi.org/10.1016/j.jvolgeores.2009.02.006.

Leaney, W.S., 2014. Microseismic source inversion in anisotropic media. PhD Thesis. Univ. British Columbia.

Menke, W., Levin, V., Sethi, R., 1995. Seismic attenuation in the crust at the mid-Atlantic plate boundary in south-west Iceland. Geophys. J. Int. 122 (1), 175–182. https://doi.org/10.1111/j.1365-246x.1995.tb03545.x.

Minson, S.E., Dreger, D.S., Bürgmann, R., Kanamori, H., Larson, K.M., 2007. Seismically and geodetically determined nondouble-couple source mechanisms from the 2000 Miyakejima volcanic earthquake swarm. J. Geophys. Res. 112, B10308. https://doi.org/10.1029/2006JB004847.

Nettles, M., Ekström, G., 1998. Faulting mechanism of anomalous earthquakes near Bárdarbunga Volcano, Iceland. J. Geophys. Res. 103 (B8), 17973–17983.

Oliva, S.J., Ebinger, C.J., Wauthier, C., Muirhead, J.D., Roecker, S.W., Rivalta, E., Heimann, S., 2019. Insights into fault-magma interactions in an early-stage continental rift from source mechanisms and correlated volcano-tectonic earthquakes. Geophys. Res. Lett. 46, 2065–2074. https://doi.org/10.1029/2018GL080866.

Passarelli, L., Heryandoko, N., Cesca, S., Rivalta, E., Rasmid, S., Rohadi, S., Dahm, T., Milkereit, C., 2018. Magmatic or not magmatic? The 2015-2016 seismic swarm at the long-dormant Jailolo volcano, West Halmahera, Indonesia. Front. Earth Sci. 6, 79. https://doi.org/10.3389/feart.2018.00079.

Rubin, A.M., 1992. Dike-induced faulting and graben subsidence in volcanic rift zones. J. Geophys. Res., Solid Earth 97 (B2), 1839–1858. https://doi.org/10.1029/91jb02170.

Shuler, A., Ekström, G., 2009. Anomalous earthquakes associated with Nyiragongo Volcano: observations and potential mechanisms. J. Volcanol. Geotherm. Res. 181 (3–4), 219–230. https://doi.org/10.1016/j.jvolgeores.2009.01.011.

Sigmundsson, F., Hooper, A., Hreinsdóttir, S., Vogfjörd, K.S., Ófeigsson, B.G., Heimisson, E.R., Eibl, E.P.S., 2014. Segmented lateral dyke growth in a rifting event at Bárðarbunga volcanic system, Iceland. Nature 517 (7533), 191–195. https://doi.org/10.1038/nature14111.

Singh, S.C., Crawford, W.C., Carton, H., Seher, T., Combier, V., Cannat, M., Canales, J.P., Düsünür, D., Javier Escartin, J., Miranda, J.M., 2006. Discovery of a magma chamber and faults beneath a Mid-Atlantic Ridge hydrothermal field. Nature 442 (31), 1029–1032. https://doi.org/10.1038/nature05105.

Sinha, M.C., Navin, D.A., MacGregor, L.M., Constable, S., Peirce, C., White, A., Heinson, G., Inglis, M.A., 1997. Evidence for accumulated melt beneath the slow-spreading Mid-Atlantic Ridge. Philos. Trans. R. Soc. Lond. A 355, 233–253. https://doi.org/10.1098/rsta.1997.0008.

Šílený, J., Hill, D.P., Eisner, L., Cornet, F.H., 2009. Non-double-couple mechanisms of microearthquakes induced by hydraulic fracturing. J. Geophys. Res. 114, B08307. https://doi.org/10.1029/2008JB005987.

Stefánsson, R., Böðvarsson, R., Slunga, R., Einarsson, P., Jakobsdóttir, S.S., Bungum, H., Gregersen, S., Havskov, J., Hjelme, J., Korhonen, H., 1993. Earthquake prediction research in the South Iceland seismic zone and the SIL project. Bull. Seismol. Soc. Am. 83, 696–716.

Templeton, D.C., Dreger, D.S., 2006. Non-double-couple earthquakes in the Long Valley volcanic region. Bull. Seismol. Soc. Am. 96 (1), 69–79. https://doi.org/10.1785/0120040206.

Tentler, T., Temperley, S., 2007. Magmatic fissures and their systems in Iceland: a tectonomagmatic model. Tectonics 26, TC5019. https://doi.org/10.1029/2006TC002037.

Thordarson, T., Larsen, G., 2007. Volcanism in Iceland in historical time: volcano types, eruption styles and eruptive history. J. Geodyn. 43, 118–152. https://doi.org/10.1016/j.jog.2006.09.005.

Trippanera, D., Ruch, J., Acocella, V., Rivalta, E., 2015. Experiments of dike-induced deformation: insights on the long-term evolution of divergent plate boundaries. J. Geophys. Res. 120 (10), 6913–6942.

Vavryčuk, V., 2011a. Principal earthquakes: theory and observations from the 2008 West Bohemia swarm. Earth Planet. Sci. Lett. 305, 290–296. https://doi.org/10.1016/j.epsl.2011.03.002.

Vavryčuk, V., 2011b. Tensile earthquakes: theory, modeling, and inversion. J. Geophys. Res. 116 (B12), B12320. https://doi.org/10.1029/2011JB008770.

Vavryčuk, V., 2015. Moment tensor decompositions revisited. J. Seismol. 19 (1), 231–252. https://doi.org/10.1007/s10950-014-9463-y.

Vavryčuk, V., Hrubcová, P., 2017. Seismological evidence of fault weakening due to erosion by fluids from observations of intraplate earthquake swarms. J. Geophys. Res., Solid Earth 122 (5), 3701–3718. https://doi.org/10.1002/2017JB013958.

Vavryčuk, V., Adamová, P., Doubravová, J., Jakoubková, H., 2017. Moment tensor inversion based on the principal component analysis of waveforms: method and application to microearthquakes in West Bohemia, Czech Republic. Seismol. Res. Lett. 88 (5), 1303–1315. https://doi.org/10.1785/0220170027.

Vavryčuk, V., Adamová, P., Doubravová, J., Ren, Y., 2021. Mapping stress and fluids on faults by nonshear earthquakes. J. Geophys. Res., Solid Earth 126, e2020JB021287. https://doi.org/10.1029/2020JB021287.

Waldhauser, F., Ellsworth, W.L., 2000. A double-difference earthquake location algorithm: method and application to the Northern Hayward fault, California. Bull. Seismol. Soc. Am. 90 (6), 1353–1368.

Willemann, R.J., 1993. Cluster analysis of seismic moment tensor orientations. Geophys. J. Int. 115, 617–634.

Yu, Ch., Vavryčuk, V., Adamová, P., Bohnhoff, M., 2018. Moment tensors of induced microearthquakes in The Geysers geothermal reservoir from broadband seismic recordings: implications for faulting regime, stress tensor and fluid pressure. J. Geophys. Res., Solid Earth 123, 8748–8766. https://doi.org/10.1029/2018JB016251.

Yu, Ch., Vavryčuk, V., Adamová, P., Bohnhoff, M., 2019. Frequency-dependent moment tensors of induced microearthquakes. Geophys. Res. Lett. 46, 6406–6414. https://doi.org/10.1029/2019GL082634.